PHYSICAL REVIEW FLUIDS **5**, 014006 (2020)

Magnetoelastic pattern formation in field-responsive fluids

Pedro O. S. Livera [*] and José A. Miranda [†]
Departamento de Física, Universidade Federal de Pernambuco, Recife, Pernambuco 50670-901, Brazil

(Received 24 October 2019; published 31 January 2020)

We study the development of interfacial magnetoelastic patterns when an initially circular droplet of a field-activated fluid (ferrofluid, or a magnetorheological fluid), surrounded by a nonmagnetic fluid, is subjected to a radial magnetic field in a Hele-Shaw cell. Elasticity takes effect when the fluids are brought into contact and, due to a chemical reaction, the interface separating them becomes a gel-like elastic layer. By modeling the interface as an elastic membrane having a curvature-dependent bending rigidity, a perturbative mode-coupling theory is employed to investigate the weakly nonlinear dynamics of the system. In this context, we examine how the interface responds to the influence of magnetic, elastic, and yield stress forces. Our findings support the relevance of a curvature weakening effect, in the sense that magnetoelastic fingering structures tend to arise and protrude in regions of lower bending rigidity. We contrast the magnetoelastic patterns with the corresponding usual shapes of magnetic fluid interfaces without bending rigidity, but with surface tension.

DOI: 10.1103/PhysRevFluids.5.014006

I. INTRODUCTION

Magnetic-field-responsive fluids, such as ferrofluids, and magnetorheological (MR) fluids are soft matter materials that conveniently combine fluidity attributes of liquids and magnetic properties of solids. Ferrofluids are colloidal suspensions of monodomain nanometer-size magnetic particles suspended in a nonmagnetic solvent [1,2]. Most ferrofluids are Newtonian fluids and do not tend to form particle chains when subjected to an applied magnetic field. On the other hand, MR fluids are suspensions of much bigger (micrometer-size) magnetic particles in a nonmagnetic carrier fluid [3–5]. In contrast to ferrofluids, MR fluids particles are multidomain and have the tendency to produce long chains under the presence of an external magnetic field. This responsive behavior leads to a rheological change of MR fluids from a liquid to a solidlike state. Consequently, and differently from ferrofluids, MR fluids are notably non-Newtonian, presenting a distinguishing magnetic-field-dependent yield stress [6–8].

The peculiar hydrodynamic and magnetic properties of ferrofluids and MR fluids make them remarkable materials to study a variety of interfacial instabilities and pattern formation processes [9,10]. This is particularly true for the case of spatially confined systems, where a magnetic fluid droplet is surrounded by a nonmagnetic fluid and placed in the narrow, effectively two-dimensional space between two parallel glass plates of a Hele-Shaw cell [11,12]. Depending on the nature of the magnetic fluid and on the symmetry properties of the applied magnetic field, various pattern morphologies can be produced. While multiply branched, labyrinth-type structures arise under the action of a perpendicularly applied magnetic field [13–16], polygon-shaped and starfishlike patterns emerge if a radial field is applied in the plane of the Hele-Shaw cell [17–19]. Moreover, if the

---

[*] pedro.oslivera@outlook.com
[†] jme@df.ufpe.br

applied field is an in-plane AC rotating magnetic field, unique spiral shapes are formed [20]. On the other hand, if the positions of the fluids are swapped and an in-plane azimuthal magnetic field produced by a current-carrying wire is applied, one observes yet another family of shapes ranging from regular *n*-fold patterns having bulbous fingers to considerably intricate, ramified fingering arrangements [21–23]. In all these systems [13–23] the shape of the resulting patterns is determined by the interplay of magnetic, surface tension, and yield stress forces.

Interesting possibilities for these magnetic-field-activated fluid systems confined in Hele-Shaw cells are offered if one considers the inclusion of an extra physical ingredient: the action of elastic forces at the interface. Recent experiments using two nonmagnetic reacting fluids in a Hele-Shaw cell show that when the fluids are put in contact, a chemical reaction occurs and the fluid-fluid interface becomes a gel-like elastic layer [24]. In fact, there are several other experimental Hele-Shaw systems involving nonmagnetic fluids which exhibit different phenomena and unusual fingering patterns caused by chemical reactions [25–28], precipitation reactions and chemical gardens [29–32], and gel-producing reactions [33,34].

The appealing experimental results reported in Ref. [24] inspired some theoretical studies about the detected elastic fingering phenomena. Linear stability analysis [35], weakly nonlinear theory [36], and sophisticated boundary integral numerical simulations [37] have examined the problem theoretically. These theoretical investigations have demonstrated that the basic physics of the reactive flow system experimentally examined in Ref. [24] can be properly described by a model considering the interface as a thin elastic membrane. Consistency between theory and experiments is obtained when the elastic membrane is modeled as having a curvature-dependent bending rigidity whose value decreases as the local interfacial curvature increases [35–37].

Motivated by the experimental and theoretical findings reported in Refs. [24–37] regarding pattern formation in reactive fluids and the presence of an elastic membrane separating fluids in Hele-Shaw flows, in this work we investigate a magnetoelastic version of such a problem. We consider that a magnetic fluid (a ferrofluid, or a MR fluid) droplet is surrounded by a nonmagnetic fluid and subjected to an applied in-plane radial magnetic field. The elastic gel-like magnetic fluid interface we model is originated by a chemical reaction as in the case already studied experimentally [24] and theoretically [35–37] for nonmagnetic fluid flows in Hele-Shaw cells. Additionally, as in Refs. [35–37], we assume that the fluid-fluid boundary is a thin elastic layer presenting a curvature-dependent bending rigidity. This opens up the possibility of studying still unexplored pattern-forming phenomena in such confined magnetoelastic fluid system, by taking into account the influence of magnetic, elastic, and yield stress effects at the interface.

It should be stressed that the impact of elastic interface effects on the dynamics and pattern formation of magnetic fluids in Hele-Shaw geometry is a considerably unexploited research area. One exception is a recent work [38] which examined the formation of wrinkling and folding patterns in a confined ferrofluid droplet having an elastic boundary subjected to a radial magnetic field. However, the work carried out in Ref. [38] utilized a simplified theoretical description of the problem; in particular, the elastic interface was assumed to have a constant bending rigidity. In addition, the perturbative study performed in Ref. [38] was restricted to a simple linear stability analysis. More complicated fully nonlinear aspects of the patterns have been obtained in a nonperturbative manner through the evaluation of stationary exact solutions for the interface shape by utilizing a vortex sheet approach.

This paper expands the work carried out in Ref. [38] in several directions. First, as in Refs. [35–37], we now use a more realistic and better established theoretical modeling for the elastic interface and consider that it has a curvature-dependent bending rigidity. Moreover, in contrast to what was done in Ref. [38], we go beyond the linear regime and perform a second-order weakly nonlinear analysis of the system. This is a very important point since the inclusion of nonlinear effects is simply essential to allow one to extract important information about the morphology of the patterns [39]. It should also be mentioned that, contrary to what has been executed in Ref. [38], which tried to assess nonlinear morphological information from stationary exact solutions of the problem, here we get useful insight into the shape of the patterns via the establishment of

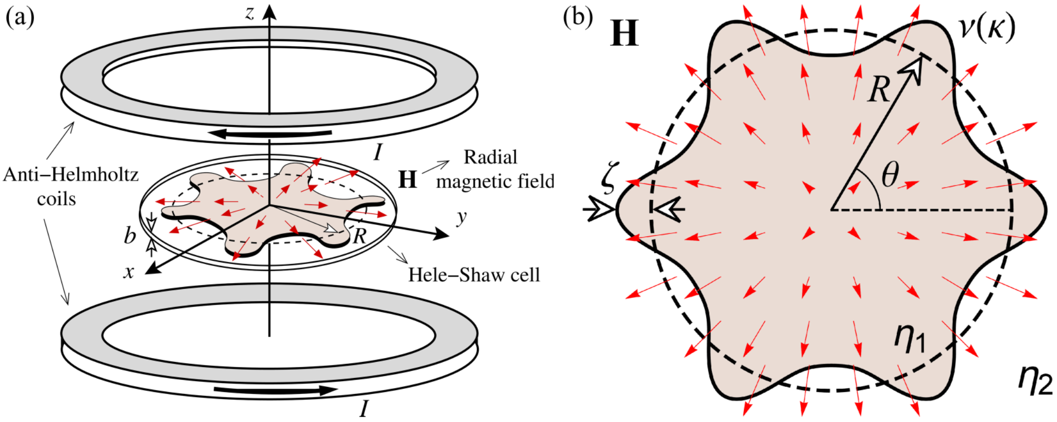

FIG. 1. (a) Schematic illustrating the perspective view of the anti-Helmholtz magnetic-field arrangement in a Hele-Shaw cell of gap thickness b. The electric currents I in the coils are equal and flow in opposite directions, producing a magnetic field $\mathbf{H}$ [Eq. (1)] pointing radially outward in the plane of the cell ($z = 0$ plane). The inner fluid (fluid 1) is a magnetic fluid and the outer fluid (fluid 2) is nonmagnetic. Initially, the magnetic fluid droplet has a circular shape of radius R (dashed curve), but may deform (solid curve) due to the action of $\mathbf{H}$. (b) Schematic depicting the top view of the system. The interface perturbation amplitude is denoted by $\zeta = \zeta(\theta, t)$ [Eq. (4)], where θ is the azimuthal angle. The interface is elastic and has a curvature-dependent bending rigidity $\nu(\kappa)$ [Eq. (2)]. The viscosity of the inner (outer) fluid is η_1 (η_2).

time-evolving nonlinear solutions. This is also a significant distinction, since, while the stability of the stationary vortex sheet solutions obtained in Ref. [38] is still an open question [38,40], the stability of the time-evolving weakly solutions we get in this work can been directly verified by the saturation of the Fourier mode amplitudes. Furthermore, as opposed to Ref. [38], which is limited to the study of ferrofluids, in this work we also consider the case in which the magnetic liquid is a MR fluid.

II. PHYSICAL PROBLEM AND GOVERNING EQUATIONS

The geometry of the problem is schematically illustrated in Fig. 1: A magnetic fluid (ferrofluid, or MR fluid) droplet of radius R and viscosity η_1 is surrounded by a nonmagnetic fluid of viscosity η_2. Both fluids are incompressible and are confined in a Hele-Shaw cell of thickness b. We consider the action of a radial magnetic field given by [17,41]

$$\mathbf{H} = H_0 r \hat{\mathbf{e}}_r, \tag{1}$$

where r is the radial distance from the origin of the coordinate system (located at the center of the droplet), H_0 is a constant, and $\hat{\mathbf{e}}_r$ is a unit vector in the radial direction. The radial magnetic field is produced by a pair of identical Helmholtz coils whose electric currents are equal and flow in opposite directions [Fig. 1(a)]. This is commonly known as the anti-Helmholtz configuration. For experimental realizations of such a radial magnetic-field arrangement see, for instance, Refs. [42–46]. The Hele-Shaw cell is located at the mid-distance between the coils, in such a way that the radial magnetic field is coplanar to it. A magnetic body force $\sim\nabla H$, where $H = |\mathbf{H}|$ is the local magnetic-field intensity, acts on the magnetic fluid pointing in the outward radial direction. As the applied radial magnetic field given by Eq. (1) has a natural nonzero gradient, we take it as the main local field contribution to the magnetic body force. Therefore, in this paper we do not consider the influence of the demagnetizing field [1,2]. As already discussed in Ref. [38], within the scope of our radial magnetic-field problem, demagnetizing effects can be safely neglected.

We follow Refs. [35–37] and consider that the interface separating the fluids is a thin elastic membrane presenting a curvature-dependent bending rigidity given by

$$\nu = \nu(\kappa) = \nu_0[Ce^{-\lambda^2\kappa^2} + 1 - C], \tag{2}$$

where

$$\kappa = \frac{r^2 + 2\left(\frac{\partial r}{\partial \theta}\right)^2 - r\frac{\partial^2 r}{\partial \theta^2}}{\left[r^2 + \left(\frac{\partial r}{\partial \theta}\right)^2\right]^{3/2}} \tag{3}$$

denotes the interface curvature in the plane of the Hele-Shaw cell, with θ representing the azimuthal angle [Fig. 1(b)]. This model for $\nu(\kappa)$ is based on the fact that as the interface curves, it is expected that intermolecular bonds are broken, thus reducing the rigidity of the gel-like elastic layer. Thus, $\nu(\kappa)$ should decrease as κ is increased. In Eq. (2) ν_0 is the maximum rigidity that expresses the largest resistance to disturbances and $0 \leqslant C < 1$ is the bending rigidity fraction, which measures the fraction of intramolecular bonds broken through surface deformation. Moreover, $\lambda > 0$ represents a characteristic radius beyond which $\nu(\kappa)$ decreases substantially. Note that by setting $C = 0$ one reaches the simpler constant bending rigidity limit used in Ref. [38] for which $\nu = \nu_0$.

The interplay of magnetic, elastic, and yield stress forces may deform the interface separating the fluids. The perturbed interface shape is described as $\mathcal{R}(\theta, t) = R + \zeta(\theta, t)$, where R is the radius of the initially circular interface at $t = 0$. Here

$$\zeta(\theta, t) = \sum_{n=-\infty}^{+\infty} \zeta_n(t) \exp(in\theta) \tag{4}$$

is the net interface perturbation with Fourier amplitudes $\zeta_n(t)$ and integer wave numbers n. Our perturbative weakly nonlinear approach keeps terms up to the second order in ζ. Mass conservation imposes that the zeroth mode is written in terms of the other modes as $\zeta_0 = -(1/2R)\sum_{n\neq 0}|\zeta_n(t)|^2$ [39]. Our main goal in this section is to derive a mode-coupling differential equation that describes the time evolution of the interfacial amplitudes $\zeta_n(t)$ at the onset of nonlinear effects.

Under the spatially confined Hele-Shaw flow conditions of our problem, the effectively two-dimensional dynamics of the magnetic fluid droplet can be described by a modified Darcy law for the gap-averaged velocity [6–8,13,14,47]

$$\mathbf{v}_j = -\frac{b^2}{12\eta_j}\left[\nabla\Pi_j + \frac{3\sigma_y(H)}{b}\hat{\mathbf{e}}_r\right], \tag{5}$$

where $j = 1$ ($j = 2$) labels the inner (outer) fluid. In Eq. (5) the gap-averaged generalized pressure is defined as [15]

$$\Pi_j = \frac{1}{b}\int_{-b/2}^{+b/2} [P_j - \Psi]dz, \tag{6}$$

where P_j is the three-dimensional pressure,

$$\Psi = \frac{\mu_0\chi H^2}{2} \tag{7}$$

represents a magnetic pressure [1], and μ_0 denotes the magnetic permeability of free space. In Eq. (7) we used the linear relationship $\mathbf{M} = \chi\mathbf{H}$, with $M = |\mathbf{M}|$ the magnetization of the magnetic fluid and χ its magnetic susceptibility. Note that for the nonmagnetic outer fluid $\chi = 0$ and $\Psi = 0$.

The second term in square brackets on the right-hand side of Eq. (5) expresses the contribution of a magnetic-field-dependent yield stress which is given by [3–5,7,8]

$$\sigma_y(H) = \sigma_{y0} + \alpha H^2, \tag{8}$$

where σ_{y0} stands for the yield stress in the absence of the magnetic field and α is a constant that depends on the material properties of the magnetic fluid, being proportional to the particle volume fraction [5]. Based on the symmetry of the applied magnetic field, we consider the prevalent yielding occurring along the radial direction. Note that, by setting $\sigma_y(H) = 0$ in Eq. (5), the yield stress term vanishes and one recovers the usual Darcy law for Newtonian ferrofluids [13–17].

It should be noted that the derivation of the generalized Darcy law given by Eq. (5) (see Refs. [7,18,47] and references therein) uses the Bingham model that presents a yield stress limit which must be exceeded before significant deformation can occur. Since we are interested in examining the interface destabilization process and the flow provoked by the applied magnetic field, we consider the regime where magnetic and viscous forces prevail over the stabilizing role of the yield stress. In this framing, flow is facilitated and nontrivial, i.e., noncircular, magnetoelastic patterns arise. This is the reason why Eq. (5) does not seem to work in the limit of $\mathbf{H} = 0$ with a finite yield stress for which the interface is perfectly stable and circular. However, note that this does not lead to any inconsistencies regarding the stability analysis of the problem: As expected, in the limit $N_B \to 0$ in Eq. (13) the yield stress effect is clearly stabilizing.

Since the field-dependent yield stress term [second term in square brackets of Eq. (5)] can be expressed as a gradient of some scalar function, the velocity field is irrotational in the bulk and we can state our problem in terms of velocity potentials ϕ_j, where $\mathbf{v}_j = -\nabla\phi_j$. Thus, from Eq. (5) and the incompressibility condition $\nabla \cdot \mathbf{v}_j = 0$ it can be verified that the potentials ϕ_j obey Laplace's equation. These velocity potentials can be written as

$$\phi_j(r,\theta) = \sum_{n\neq 0} \phi_{jn}(t)\left(\frac{r}{R}\right)^{(-1)^{(j+1)}|n|} \exp(in\theta). \tag{9}$$

Nonetheless, we still need to include the contributions coming from the elastic nature of the interface. In order to do that, as in Refs. [35–37] we consider a generalized Young-Laplace pressure boundary condition, which expresses the pressure jump across the perturbed interface as

$$\begin{aligned}(p_1 - p_2)|_{r=\mathcal{R}} = {}& \tfrac{1}{2}\nu'''\kappa^2\kappa_s^2 + \nu''\left(3\kappa\kappa_s^2 + \tfrac{1}{2}\kappa^2\kappa_{ss}\right) + \nu'\left(\tfrac{1}{2}\kappa^4 + 3\kappa_s^2 + 2\kappa\kappa_{ss}\right)\\ &+ \nu\left(\tfrac{1}{2}\kappa^3 + \kappa_{ss}\right) - \tfrac{1}{2}\mu_0(\mathbf{M}\cdot\mathbf{n})^2.\end{aligned} \tag{10}$$

As far as the mathematical origin of Eq. (10) is concerned, it can be obtained by minimizing a Helfrich-like energy functional (a measure of the energy of the elastic interface separating the two fluids) with a curvature-dependent bending rigidity. For a more detailed account of the derivation of Eq. (10) the interested reader is referred to Refs. [35,36].

In Eq. (10) the primes indicate derivatives with respect to the curvature κ, while the subscripts of κ indicate derivatives with respect to the arc length s. Note that Eq. (10) differs significantly from the traditional Young-Laplace condition applied to immiscible nonreactive fluids in Hele-Shaw cells [11,12] that is much simpler and involves only the product of κ by the surface tension σ. Similar to what is done in Refs. [35–37], we consider that elastic effects dominate the condition at the interface in such a way that surface tension effects are not considered in Eq. (10). It is also worthwhile to note that Eq. (10) is much more complex than its constant bending rigidity counterpart studied in Ref. [38], where all derivative terms with respect κ simply drop out [see Eq. (5) in Ref. [38]].

Observe that in the pressure boundary condition [Eq. (10)] there is still a term that is connected to the magnetic nature of the deforming droplet. It is precisely the last term on the right-hand side of Eq. (10), which is commonly known as the magnetic normal traction [1,2], where $\mathbf{n}$ represents the unit normal vector at the interface. This term incorporates the influence of the discontinuous normal component of the magnetization at the interface.

The problem is then fully specified with the consideration of another relevant boundary condition, known as the kinematic boundary condition. Fundamentally, it states that the normal components of each fluid's velocity are continuous at the interface [1,11,12,48]

$$\frac{\partial \mathcal{R}}{\partial t} = \left[\frac{1}{r^2}\frac{\partial \mathcal{R}}{\partial \theta}\frac{\partial \phi_j}{\partial \theta} - \frac{\partial \phi_j}{\partial r} \right] \bigg|_{r=\mathcal{R}}. \tag{11}$$

This condition holds for either fluid-fluid, fluid-elastic, or fluid-solid interfaces and implies that the fluid cannot penetrate the other medium. Equation (11) is also widely utilized in problems involving the interaction between fluids and deformable bodies [49]. In our case, the problem effectively involves three immiscible phases (the two liquids and the elastic interface). Nevertheless, since the elastic phase has negligible thickness (and thus cannot be compressed in the normal direction), the normal component of the fluid velocity must be continuous across the interface.

Finally, we have all necessary elements to derive the mode-coupling differential equation that describes the time evolution of the interfacial amplitudes $\zeta_n(t)$. We do that by following usual steps of previous weakly nonlinear studies in Hele-Shaw flows [39,50]. First, boundary conditions (10) and (11) are used to express ϕ_j [Eq. (9)] in terms of ζ_k [Eq. (4)] consistently up to second order. Then, by substituting these relations and the pressure condition (10) into the modified Darcy law (5), always keeping terms up to second order in ζ, and Fourier transforming, after some algebra, we find the *dimensionless* equation of motion for the perturbation amplitudes

$$\dot{\zeta}_n = \Lambda(n)\zeta_n + \sum_{m\neq 0}[F(n,m)\zeta_m\zeta_{n-m} + G(n,m)\dot{\zeta}_m\zeta_{n-m}], \tag{12}$$

where the overdot represents a total time derivative and

$$\Lambda(n) = |n|\left\{2N_B\chi(1+\chi) - S_0 - 3S + \tfrac{1}{2}(n^2-1)[A_1(C,\lambda)(n^2+1) + A_2(C,\lambda)]\right\} \tag{13}$$

denotes the linear growth rate. The parameter

$$N_B = \frac{\mu_0 H_0^2 R^5}{2\nu_0} \tag{14}$$

is a magnetoelastic number and measures the ratio of magnetic to elastic forces. On the other hand,

$$S_0 = \frac{3\sigma_{y0}R^4}{\nu_0 b} \tag{15}$$

and

$$S = \frac{\alpha H_0^2 R^6}{\nu_0 b} \tag{16}$$

are the parameters related to the yield stress contributions at zero and nonzero radial magnetic field, respectively. We still have that

$$A_1(C,\lambda) = Ce^{-\lambda^2}(-4\lambda^4 + 10\lambda^2 - 2) - 2(1-C) \tag{17}$$

and

$$A_2(C,\lambda) = Ce^{-\lambda^2}(8\lambda^4 - 22\lambda^2 + 5) + 5(1-C), \tag{18}$$

which are linear terms connected to the elastic nature of the interface.

The second-order mode-coupling terms are given by

$$\begin{aligned} F(n,m) = |n|[N_B\chi[1+\chi(1+m(n-m))] - 3S - \{Ce^{-\lambda^2}[B_1(n,m) + \lambda^2 B_2(n,m) \\ + \lambda^4 B_3(n,m) + 2\lambda^6 B_4(n,m)] + (1-C)B_1(n,m)\}] \end{aligned} \tag{19}$$

and

$$G(n,m) = A|n|[\text{sgn}(nm) - 1] - 1. \tag{20}$$

In the expression for the coupling function $F(n, m)$ in Eq. (19) the terms are originated from the applied radial magnetic field, field-dependent yield stress, and curvature-dependent bending rigidity contributions, respectively. The term proportional to χ^2 comes from the magnetic normal traction in the pressure jump condition [Eq. (10)]. The expressions for the functions $B_1(n, m)$, $B_2(n, m)$, $B_3(n, m)$, and $B_4(n, m)$ appearing in Eq. (19) are given in the Appendix, being related to the second-order contributions from the elastic interface.

On the other hand, the nonlinear coupling function $G(n, m)$ in Eq. (20) arises from the coupling of the perturbed flow $\dot{\zeta}$ with the interface shape perturbation ζ. It has a purely kinetic origin, having no dependence on magnetic, yield stress, or elastic effects. However, it does depend on the viscosity contrast (a dimensionless viscosity difference parameter) $A = (\eta_1 - \eta_2)/(\eta_1 + \eta_2)$, and the sgn function equals ±1 according to the sign of its argument. Notice that in Eqs. (12)–(20) lengths and velocities are rescaled by R and $\nu_0 b^2/12(\eta_1 + \eta_2)R^4$, respectively. From this point onward we use the dimensionless version of all the equations. We note that the theoretical results presented in this work utilize dimensionless quantities which are consistent with physical parameters used in Refs. [1,8,24,28,35–38,44,45].

Equation (12) is the second-order mode-coupling equation for our magnetoelastic instability problem in a Hele-Shaw cell under the presence of a radial magnetic field. This result contrasts with most findings obtained by previous theoretical studies of elastic fingering formation which focused on Hele-Shaw flows involving only nonmagnetic fluids [35–37].

Since the linear growth rate [Eq. (13)] is time independent, one can readily see from Eq. (12) that at the linear level the perturbation amplitudes $\zeta_n(t)$ grow or decay exponentially with time, i.e., $\zeta_n(t) = \zeta_n(0)\exp[\Lambda(n)t]$. The linear growth rate $\Lambda(n)$ informs about the linear stability of the system: The interface is linearly unstable (stable) to the nth mode perturbation if $\Lambda(n) > 0$ [$\Lambda(n) < 0$]. By inspecting Eq. (13) it is clear that the radial magnetic-field term proportional to N_B is destabilizing, while both yield stress terms tend to stabilize the interface in the linear regime. However, as already extensively discussed in Refs. [35–37], for a given shape-deforming mode $n \geqslant 2$ (note that for modes $n = 0$ and $n = 1$ the magnetic liquid droplet remains circular), the behavior of the curvature-dependent bending rigidity term in $\Lambda(n)$ is a bit more subtle. In the limit of constant rigidity ($C = 0$) the quantity $[A_1(C, \lambda)(n^2 + 1) + A_2(C, \lambda)]$ is negative and the bending rigidity forces tend to stabilize the interface. Roughly speaking, one can say that in this case the parameter ν_0 acts like an effective surface tension, similarly to what one has in the usual radial magnetic-field Hele-Shaw problem in the absence of elastic effects [17–19]. Nevertheless, if $0 < C < 1$, the quantity $[A_1(C, \lambda)(n^2 + 1) + A_2(C, \lambda)]$ can be positive and the effect of the curvature-dependent bending rigidity may lead to interface destabilization. However, as these elastic linear stability aspects of the problem have already been thoroughly scrutinized [35–37], in this work we concentrate our attention on nonlinear pattern-forming phenomena. More precisely, we investigate how the consideration of the second-order nonlinear terms given by Eqs. (19) and (20) might provide access to important morphological aspects of the magnetoelastic patterns during the weakly nonlinear regime.

III. WEAKLY NONLINEAR MAGNETOELASTIC PATTERNS

In this section we use Eqs. (12)–(20) to obtain perturbative solutions for the shape of confined, elastic interface magnetic fluid droplets subjected to a radial magnetic field. As in the case of Ref. [19], in this work we have that the most important morphological features of the magnetoelastic patterns can be captured by considering the coupling of a small number of participating Fourier modes. In this framework, we analyze the shapes of the resulting patterns and examine how the amplitudes of the participating modes evolve with time. Time evolution of the Fourier mode amplitudes offers a useful way to verify whether such mode amplitudes continue to grow unrestrained (as predicted by the the linear theory) or tend to saturate as time progresses. Eventual saturation of the mode amplitudes would suggest that the weakly nonlinear patterns converge to a stationary configuration. The establishment of static profiles for the elastic interface certainly reinforces the physical relevance of the perturbative weakly nonlinear solutions, indicating their dynamic stability.

The main purpose of our weakly nonlinear study is to investigate the influence of the curvature-dependent bending rigidity [Eq. (2)] on the shape of the emerging magnetoelastic fingering structures. Another important aspect to be examined is to check how the magnetoelastic patterns differ from their nonelastic counterparts [17–19]. In Refs. [17–19] elastic effects were not present and the fluid-fluid interface was regulated by surface tension forces. The comparison of the shapes assumed by elastic interface magnetic fluid patterns with the usual shapes of conventional magnetic fluid patterned structures, i.e., with no bending rigidity, but with surface tension, would highlight the effect of replacing surface tension by bending rigidity in the interfacial instabilities. All these important aspects will be investigated in Sec. III A for ferrofluids and in Sec. III B for MR fluids.

To generate the shapes of the elastic interface magnetic fluid fingering structures, we consider the nonlinear coupling of a finite number N of Fourier modes and rewrite Eq. (12) in terms of the real-valued cosine amplitudes $a_n = \zeta_n + \zeta_{-n}$. The magnetoelastic patterns and the time evolution of the cosine mode amplitudes are obtained by numerically solving the corresponding coupled nonlinear differential equations. Once this is done, the shape of the elastic interface is found by utilizing Eq. (4). Most of the magnetoelastic patterns presented in Secs. III A and III B are obtained by considering the interplay of only four ($N = 4$) participating Fourier modes: the fundamental mode n and its harmonics $2n$, $3n$, and $4n$. Amazingly enough, the inclusion of just these modes is sufficient to reproduce accurately the shape of the resulting magnetoelastic structure. Thus, including more modes will not change the ultimate shape of the elastic interface magnetic fluid patterns (this point will be discussed further in Secs. III A and III B).

Throughout this work, we assume that the fundamental mode n is given by the closest integer to the fastest growing mode $n_{\max}$, i.e., the mode of maximum linear growth rate $\Lambda(n)$, obtained by the condition $[d\Lambda(n)/dn]|_{n=n_{\max}} = 0$. We point out that although $\Lambda(n_{\max}) > 0$ drives a positive linear growth of the fundamental mode n, the other participating harmonic modes ($2n$, $3n$, and $4n$) present a negative growth rate and therefore are linearly stable. Consequently, any growth of such modes is genuinely caused by the weakly nonlinear coupling. Additionally, to ensure that the interfacial behaviors we detect in this work are spontaneously induced by the weakly nonlinear dynamics and not by artificially imposing large initial amplitudes for the harmonic modes, we always set the initial ($t = 0$) harmonic mode amplitudes to zero. This is done to avoid artificial growth of modes $2n$, $3n$, and $4n$ imposed solely by the initial conditions.

As mentioned above, in this work we consider situations dominated by a single linearly unstable mode (the fundamental mode n). However, it should be stressed that our truncated weakly nonlinear expansion works equally well in cases where more than one linearly unstable mode competes at the early nonlinear level. Actually, this issue has been analyzed some time ago in Ref. [39], where it was shown that in both scenarios the qualitative results regarding the main morphological features of the produced patterns, e.g., fingertip broadening and fingertip sharpening features, are the same. As shown in Ref. [39], while the consideration of a single linearly unstable mode leads to patterns that are quite symmetric in shape, the inclusion of sophistication involving more than one linearly unstable mode, random phases, etc., results in patterns that are not as symmetric with some fingers competing and advancing over others. Nevertheless, in both cases, i.e., by using one or more linearly unstable modes, the most relevant morphological aspects of the resulting patterns are equally revealed by the second-order mode-coupling approach.

Including the general behavior of both ferrofluids and MR fluids, our magnetoelastic problem is governed by a considerably large number of dimensionless parameters: A, χ, N_B, S_0, S, C, and λ. For the sake of clarity and understanding the most important physical effects in our problem, and without affecting the validity and relevance of our theoretical analysis, we tried to reduce a bit the number of parameters that describe the situations we investigate in this work. First, to allow some connection with the most common circumstances of existing experiments with confined magnetic fluids (see, for instance, Refs. [1,2,13–15,20]), we focus on the situation in which the inner magnetic fluid is much more viscous than the outer nonmagnetic fluid. Therefore, we assume that $\eta_1 \gg \eta_2$

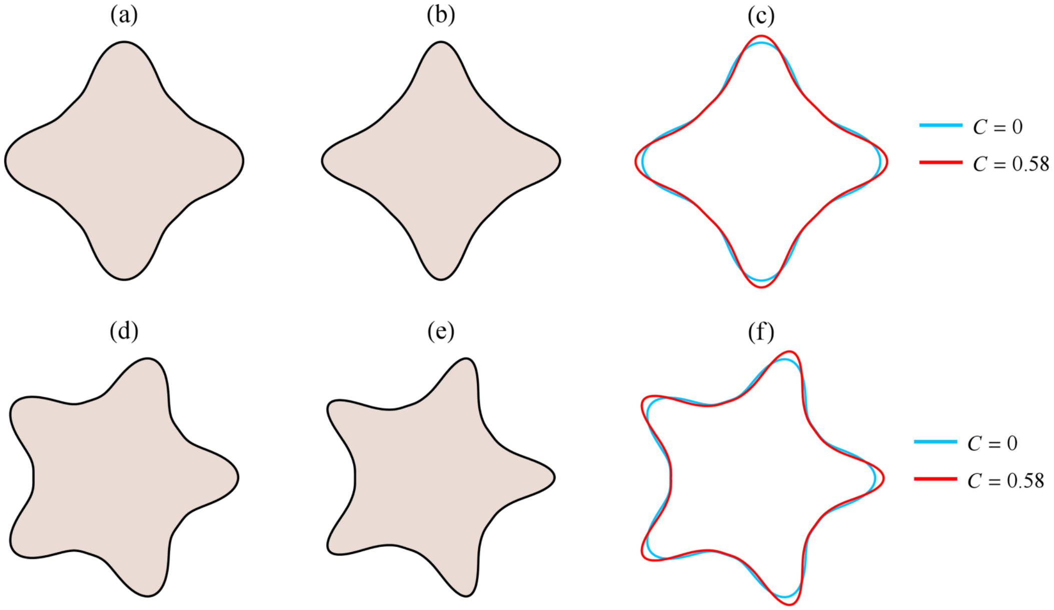

FIG. 2. Representative weakly nonlinear, elastic interface ferrofluid patterns considering the coupling of four Fourier modes n, $2n$, $3n$, and $4n$ for (a)–(c) $n = 4$, $N_B = 30$, and $\chi = 4$ and (d)–(f) $n = 5$, $N_B = 740$, and $\chi = 1$. In addition, (a) and (d) $C = 0$, (b) and (e) $C = 0.58$, and (c) and (f) for each n, the patterns for $C = 0$ and $C = 0.58$ are overlaid. The patterns are plotted for time $t = 0.005$.

so that the viscosity contrast A can be kept fixed and equal to one ($A = 1$). However, it should be stressed that the experiments performed in Refs. [1,2,13–15,20] do not consider the presence of an elastic interface. In any case, we checked that the results presented in the rest of this article remain qualitatively unchanged if other values of A are used. In addition, as long as elastic effects are concerned, we consider a small and fixed value of the characteristic radius λ ($\lambda = 0.01$) and tune elastic effects by varying the bending rigidity fraction parameter C, where $0 \leqslant C < 1$. This is done in order to keep the linear growth rate $\Lambda(n)$ bound and the fastest growing mode $n_{\max}$ unchanged while we change C.

Therefore, keeping in mind the observations given in the previous two paragraphs, in terms of relevant dimensionless parameters, we have the following scenario: If the magnetic fluid is a ferrofluid (Sec. III A), we have that $S_0 = S = 0$, and in this case we deal with only three dimensionless controlling parameters, namely χ, N_B, and C. Conversely, if the magnetic fluid is a MR fluid (Sec. III B), we do have to work with five parameters (χ, N_B, S_0, S, and C).

A. Elastic interface ferrofluid

We begin our investigation by examining Fig. 2, which depicts a typical set of weakly nonlinear, elastic interface ferrofluid patterns. Figure 2 is plotted for time $t = 0.005$, considering the coupling of four Fourier modes n, $2n$, $3n$, and $4n$. The reason for considering this specific time will be given later in this section. Since the main goal of our theory is to study the effect of the bending rigidity fraction C on the morphology of the magnetoelastic fingering patterns, the results presented in Fig. 2 focus on illustrating the most characteristic aspects of the ferrofluid droplet shapes when $C = 0$ and $C \neq 0$. Therefore, in Figs. 2(a) and 2(d) we set $C = 0$ and in Figs. 2(b) and 2(e) we take $C = 0.58$. In addition, in Figs. 2(c) and 2(f), for each of the fundamental modes n considered, the patterns for $C = 0$ and $C = 0.58$ are overlaid. This is done to facilitate comparison of the emerging shapes for these two values of C. It should be noted that, even though $0 \leqslant C < 1$, in the realm of our

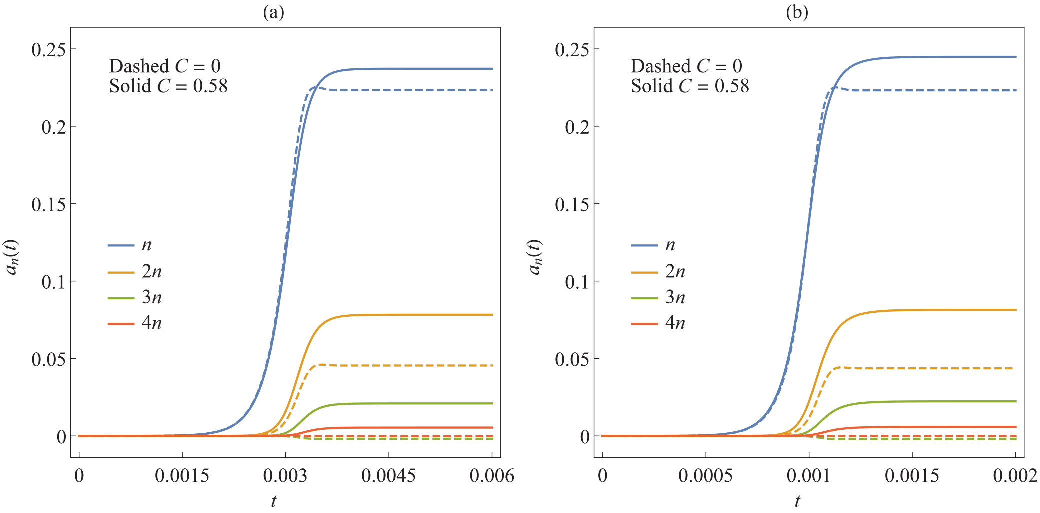

FIG. 3. Time evolution of the perturbation amplitudes $a_n(t)$, $a_{2n}(t)$, $a_{3n}(t)$, and $a_{4n}(t)$ for the patterns depicted in (a) Figs. 2(a)–2(c) for $n = 4$ and (b) Figs. 2(d)–2(f) for $n = 5$. The dashed (solid) curves take the value $C = 0$ ($C = 0.58$). It is clear that for both values of C the mode amplitudes tend to stationary values.

second-order perturbative approach, we have found that $C = 0.58$ is the maximum allowed value for the bending rigidity fraction which results in dynamically stable elastic interface ferrofluid patterns. In Figs. 2(a)–2(c) we have $n = 4$, $N_B = 30$, and $\chi = 4$. On the other hand, in Figs. 2(d)–2(f) we have that $n = 5$, $N_B = 740$, and $\chi = 1$. In Fig. 2 and in all remaining figures of this work, the initial amplitude for the fundamental mode n is taken as $a_n(t = 0) = 10^{-6}$, while the initial amplitudes for all the other (harmonic) modes are set to zero.

By inspecting the patterns in Figs. 2(a)–2(c) we observe the formation of fourfold fingered, magnetoelastic structures. It is quite evident that the pattern produced in Fig. 2(a) for $C = 0$ is distinct from the one depicted in Fig. 2(b) for $C = 0.58$. While the fingers are rounded at their tips for $C = 0$, they are sharper when $C = 0.58$. This difference in the shape of the fingers for different values of C is even more apparent when the patterns' interfaces are superimposed, as illustrated in Fig. 2(c). It is clear that the fingers generated for $C = 0.58$ not only are sharper, but also a bit longer than the ones produced when $C = 0$. The same type of behavior is observed in the fivefold structures depicted in Figs. 2(d)–2(f). In fact, we have verified the very same trend for other cases we have analyzed, using different sets of parameters (N_B, χ, and C) and other values of the fundamental mode n. Thus, the morphological features revealed in Fig. 2 are fairly representative of the general behavior presented by elastic interface ferrofluid patterns in the weakly nonlinear regime.

The interfacial shape changes induced by C for our magnetoelastic problem as portrayed in Fig. 2 are consistent with the curvature weakening effect detected in the development of elastic fingering in confined nonmagnetic fluids [35,37]. A possible physical explanation for such a behavior is given as follows. The shape dependence of the bending rigidity $\nu(\kappa)$ involves dynamical changes given by Eq. (2), which expresses the reduction of the elastic bending resistance for increasingly larger values of the local interface curvature κ. Therefore, the emergence of magnetic-field-activated interfacial elastic protuberances should be facilitated in regions of lower rigidity, i.e., regions of larger local curvature. This justifies the fact that the elastic ferrofluid fingers shown in Fig. 2 should be sharper at their tips for larger values of C.

We proceed by analyzing Fig. 3, which illustrates the time evolution of the second-order cosine amplitudes $a_n(t)$ for each of the participating Fourier modes n, $2n$, $3n$, and $4n$ used to generate the magnetoelastic patterns displayed in Fig. 2. The solid curves represent the time evolution of the amplitudes for $C = 0.58$ and the dashed curves represent the case in which $C = 0$. Figure 3(a)

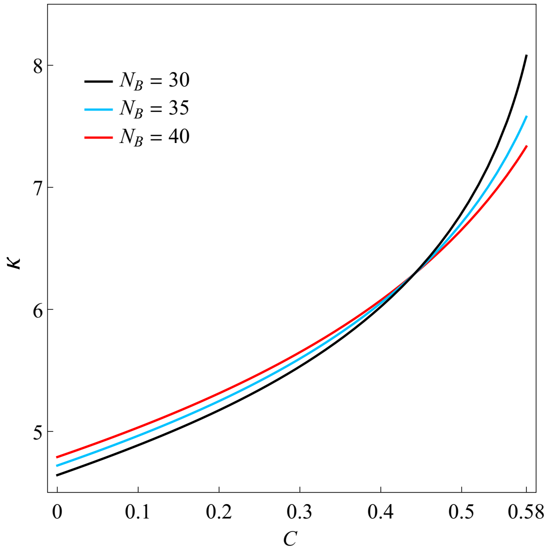

FIG. 4. Variation of the fingertip curvature κ in terms of C, for three values of the magnetoelastic number N_B: 30, 35, and 40. The remaining physical parameters are identical to the ones utilized in the fourfold patterns shown in Figs. 2(a)–2(c).

plots $a_n(t)$ versus time t for the fourfold patterns exhibited in Figs. 2(a)–2(c); Fig. 3(b) represents the equivalent behavior for the amplitudes associated with the fivefold patterns shown in Figs. 2(d)–2(f). A conspicuous feature of most of the curves depicted in Figs. 3(a) and 3(b) is the fact that, regardless of the value of C, after a sharp initial increase in intensity, the mode amplitudes eventually saturate their growth, ultimately assuming stationary values. This mode saturation behavior controls the exponential growth predicted by the purely linear theory, indicating that our second-order weakly nonlinear solutions are dynamically stable. At this point, we can justify why we have chosen the time $t = 0.005$ to plot the patterns in Fig. 2: It is simply because at this time, all the patterns shown have already reached a stationary configuration. This remark is equally valid for the MR fluid cases depicted in Fig. 6.

It is known [39] that the fundamental mode n is responsible for setting the overall shape of the patterns, i.e., the number of fingers, whose sizes are affected by the magnitude of the fundamental mode amplitude. Moreover, it is also well established [39] that the harmonic modes influence the shape of the fingers produced (for instance, determine whether the fingers are sharp or wide at their tips). In particular, the fact that the amplitude of the first harmonic mode $2n$ for $C = 0.58$ is greater than the corresponding amplitude for $C = 0$ indicates a tendency toward fingertip sharpening for larger C. These weakly nonlinear findings extracted from Fig. 3 support what is visually observed in Fig. 2: Higher values of C are associated with the formation of pattern-forming structures presenting longer and sharper fingers.

In Figs. 2 and 3 we have analyzed the behavior of the elastic interface ferrofluid patterns only for two representative values of the bending rigidity fraction C, namely, for $C = 0$ and $C = 0.58$. In Fig. 4 we extract complementary information about the system, by examining how the curvature of a fingertip κ varies for a range of values of C ($0 \leqslant C \leqslant 0.58$). In addition, in order to investigate how the magnetoelastic number N_B influences the fingertip curvature, the plot of κ in terms of C is performed for three increasingly larger values of N_B: 30, 35, and 40. The data presented in Fig. 4 use the physical parameters utilized to obtain the fourfold structures depicted in Figs. 2(a)–2(c). The most noticeable aspect of Fig. 4 is the fact that, for a given N_B, the curvature κ increases with C. However, also interesting is the combined role of C and N_B to determine the sharpness of the

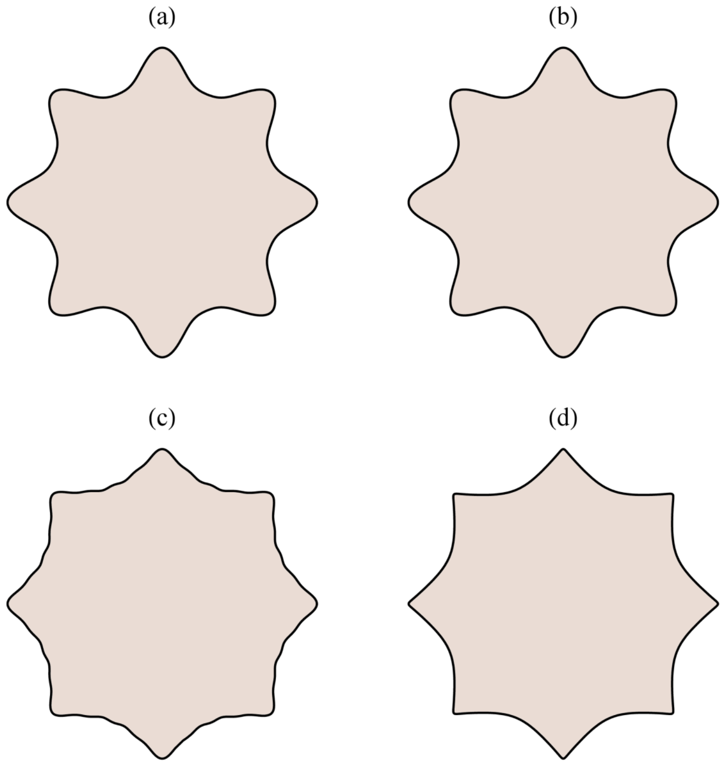

FIG. 5. Comparison of the typical ferrofluid, stationary patterned shapes when at the boundary separating the fluids there is (a) and (b) an elastic bending rigidity or (c) and (d) an interfacial surface tension. These patterns are generated by using (a) and (c) four ($N = 4$) and (b) and (d) 40 ($N = 40$) participating modes.

fingertip: Initially, for smaller values of C, one can see that sharper fingers are obtained for larger values of N_B. However, this behavior is modified as the value of C is augmented: After C reaches a certain magnitude (in Fig. 4, for $C \geqslant 0.44$) the situation rendering more acute fingers is precisely the one for smaller N_B. This means that, even though both C and N_B contribute to favor the formation of sharper fingers, if the magnitude of C is high enough, the role of the bending rigidity fraction takes over and determines the behavior of the fingertip. Analogous results are obtained for the fivefold patterns shown in Figs. 2(d)–2(f).

We close this section by addressing two important issues. First, we investigate the influence of the number of participating Fourier modes N in determining the shape of the interface at the onset of nonlinear effects. In addition, we examine how the shapes of the characteristic elastic interface ferrofluid patterns investigated in this work compare with the typical shapes obtained when a nonelastic interface ferrofluid droplet, i.e., with no bending rigidity but with surface tension, is subjected to an applied radial magnetic field, as studied in Refs. [17,19]. This is done in Fig. 5, which illustrates typical eightfold ($n = 8$) elastic interface ferrofluid, stationary patterns for $C = 0$, $\chi = 0.45$, and $N_B = 15400$ [Figs. 5(a) and 5(b)]. This specific value of C has been used since when $C = 0$ one gets an elastic interface with constant bending rigidity ν_0 [Eq. (2)], which is the closest analog of the usual surface tension situation.

The only difference between the way the patterns in Fig. 5 have been produced is that four participating Fourier modes ($N = 4$) are used in Fig. 5(a) (n, $2n$, $3n$, and $4n$), while 40 participating modes ($N = 40$) are utilized in Fig. 5(b) (n, $2n$, $3n$, $\ldots$, $40n$). In contrast, Figs. 5(c) and 5(d) depict characteristic eightfold patterns generated when elastic effects are absent, i.e., there is no bending rigidity at the interface, but there exists a surface tension σ at the fluid-fluid interface [17,19]. These surface-tension-regulated patterns have been obtained by using $\chi = 0.45$ and $N_B^\sigma = 150$, where N_B^σ represents a magnetic Bond number that measures the ratio of magnetic to capillary forces [17,19]. Once again, the single difference in the way these patterns are generated is that $N = 4$ in Fig. 5(c) and $N = 40$ in Fig. 5(d). It should be noted that the appreciably different numerical values used for N_B and N_B^σ result from the fact that in the surface tension case, although lengths are rescaled by R as in our current magnetoelastic problem, velocities are instead rescaled by $\sigma b^2[12(\eta_1 + \eta_2)R^2]$.

First, let us discuss the role played by the number of participating modes N used to produce the patterns in Fig. 5. By contrasting the elastic interface ferrofluid patterns [Figs. 5(a) and 5(b)] we can immediately see that they are simply indistinguishable, despite the fact that just four participating modes are present in Fig. 5(a), while 40 modes are used to get Fig. 5(b). This indicates that, in the elastic case, the four-mode scheme already captures all the essential morphological features of the stationary patterns. We have verified that this happens because in the case of an elastic interface ferrofluid the magnitude of the perturbation amplitudes drops very quickly as the number of participating modes is increased. As a consequence, adding more participating modes does not make much difference.

Nevertheless, the scenario is a bit different in the cases shown [Figs. 5(c) and 5(d)] in which bending rigidity is not present and surface tension takes over. It is evident that the interface pattern shown in Fig. 5(c) is different from the one displayed in Fig. 5(d). Although both structures have eight protrusions, in Fig. 5(c) the fingertips (vertices) are rounded and separated by undulating edges, while in Fig. 5(d) one observes the formation of cusped tips connected by smooth concave-shaped edges. Therefore, even though Fig. 5(c) correctly captures the overall shape of the surface tension pattern, a more accurate description of the interface can only be obtained as a greater number of participating Fourier modes are included. Consequently, as opposed to what happens in the elastic interface ferrofluid case [Figs. 5(a) and 5(b)], in the surface tension situation [Figs. 5(c) and 5(d)] the proper stationary pattern morphology is captured if 40 modes are used.

We go on by commenting on the effect of replacing surface tension by bending rigidity in the ferrofluid instabilities. It turns out that the shapes of the elastic interface ferrofluid patterns are significantly different from the ones obtained when elastic effects are not present, but interfacial surface tension forces act. A comparison can be performed most efficiently by contrasting Figs. 5(b) and 5(d): The very sharp cusped finger ends emerging in the surface tension starfishlike pattern [Fig. 5(d)] are replaced by considerably smoother and more rounded fingertips in the elastic interface ferrofluid structure [Fig. 5(b)].

A physical justification for the origin of the very pointy tips presented on the surface tension pattern depicted in Fig. 5(d) can be given as follows. Despite the action of the interfacial surface tension at the fluid-fluid interface (which favors the formation of rounded tips), as the applied magnetic field [Eq. (1)] increases with radial distance and because the magnetic traction term proportional to $(\hat{\mathbf{e}}_r \cdot \mathbf{n})^2$ in Eq. (10) is maximized as $\mathbf{n}$ is collinear to $\hat{\mathbf{e}}_r$, once a finger protuberance is formed, the growing starfishlike structures tend to become shaper and sharper at their corners. Such cusped patterns do not appear in the elastic interface case [Fig. 5(b)] due to the greater rigidity of the elastic layer separating the fluids.

B. Elastic interface MR fluid

In this section we turn our attention to the study of the elastic interface MR fluid patterns. We initiate our discussion by examining Fig. 6, which presents illustrative examples of such confined magnetic-field-induced elastic interface structures. As in the case of Sec. III A, these weakly nonlinear patterns are produced by considering the interplay of four modes n, $2n$, $3n$, and $4n$. In Figs. 6(a) and 6(d) $C = 0$ and in Figs. 6(b) and 6(e) $C = 0.99$. Finally, in Figs. 6(c) and 6(f), for each n, the patterns for $C = 0$ and $C = 0.99$ are superimposed. Notice that since yield stress effects present in the MR fluid are rather stabilizing, we managed to assess and explore high values of the bending rigidity fraction parameter C, i.e., $C = 0.99$. In Figs. 2(a)–2(c) we have that $n = 4$, $N_B = 58$, $\chi = 4$, $S_0 = 0$, and $S = 350$. Moreover, in Figs. 2(d)–2(f) we

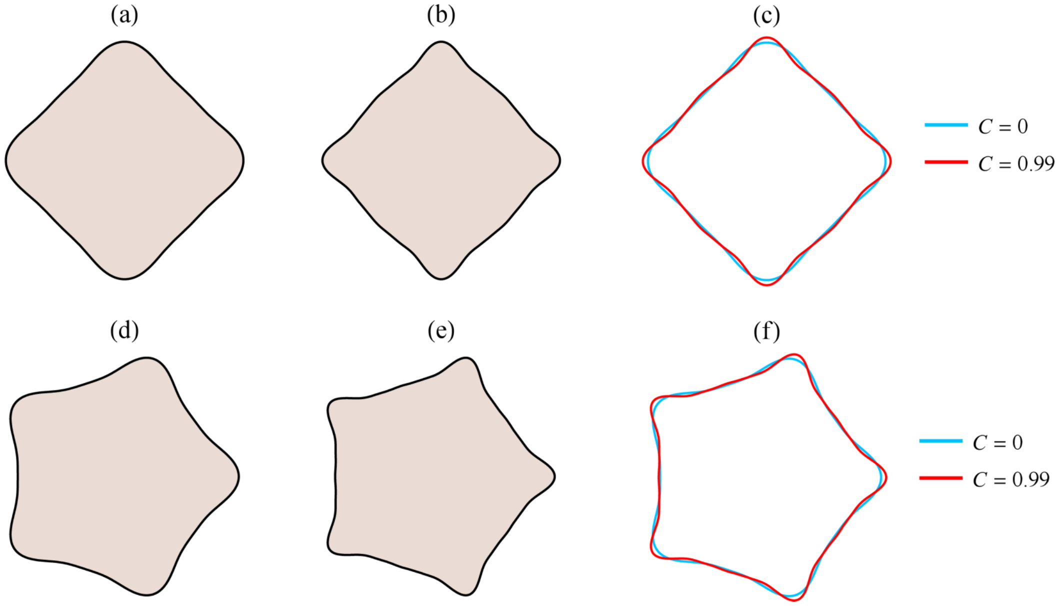

FIG. 6. Representative weakly nonlinear, elastic interface MR fluid patterns considering the coupling of four Fourier modes n, $2n$, $3n$, and $4n$ for (a)–(c) $n = 4$, $N_B = 58$, $\chi = 4$, $S_0 = 0$, and $S = 350$ and (d)–(f) $n = 5$, $N_B = 1500$, $\chi = 1$, $S_0 = 0$, and $S = 1000$. In addition, (a) and (d) $C = 0$, (b) and (e) $C = 0.99$, and (c) and (f) for each n, the patterns for $C = 0$ and $C = 0.99$ are overlaid. As in the case of Fig. 2, here the patterns are plotted for time $t = 0.005$.

have that $n = 5$, $N_B = 1500$, $\chi = 1$, $S_0 = 0$, and $S = 1000$. All the shapes are displayed for time $t = 0.005$.

By checking Fig. 6 one readily observes that the elastic interface MR patterns are dissimilar from their ferrofluid counterparts illustrated in Fig. 2. While the elastic interface ferrofluid patterns of Fig. 2 present starlike shapes and have prominent fingers, the MR fluid structures are more polygonal-like, revealing the formation of relatively small stubby fingers. The stubby nature of the elastic interface MR fluid patterns can be attributed to the stabilizing effects introduced by the magnetic-field-dependent yield stress parameter S which tends to hold most of the MR fluid material close to the center of the droplet. This field-regulated yield stress effect makes the elastic interface MR fluid patterns look more “swollen” than the corresponding elastic ferrofluid shapes.

Further examination of Fig. 6 give us information about the changes occurring in the morphology of the fingering structures when C is modified. One can quickly verify that when $C = 0$ [Figs. 6(a) and 6(d)] polygonal-like shapes containing rounded fingers located at the vertices are obtained. However, it is clear that another class of patterns arises when $C = 0.99$ [Figs. 6(b) and 6(e)]: Even though the patterns are still polygonal in shape, their fingertips are notably sharper than the ones generated when $C = 0$. Furthermore, by scrutinizing Figs. 6(c) and 6(f) one can see that the lengths of the fingers for $C = 0.99$ are a bit longer than the fingers produced when $C = 0$. These observations regarding the influence of C on the finger shapes and lengths of elastic interface MR fluid patterns are similar to those found in the case of elastic interface ferrofluids (Fig. 2). Therefore, we can say that the curvature weakening effect that took place in the elastic ferrofluid situation still persists in the case of elastic MR fluids. Then, in Fig. 6, longer fingers having sharper tips are supposed to emerge for larger values of the bending rigidity fraction parameter C. As in the case of elastic ferrofluids, we have verified the very same tendency for other elastic interface MR fluid cases we have analyzed, using different sets of parameters (N_B, χ, C, S_0, and S) and other values of the fundamental mode n. If values of $S_0 \neq 0$ are used, the overall shape of the patterns is not changed,

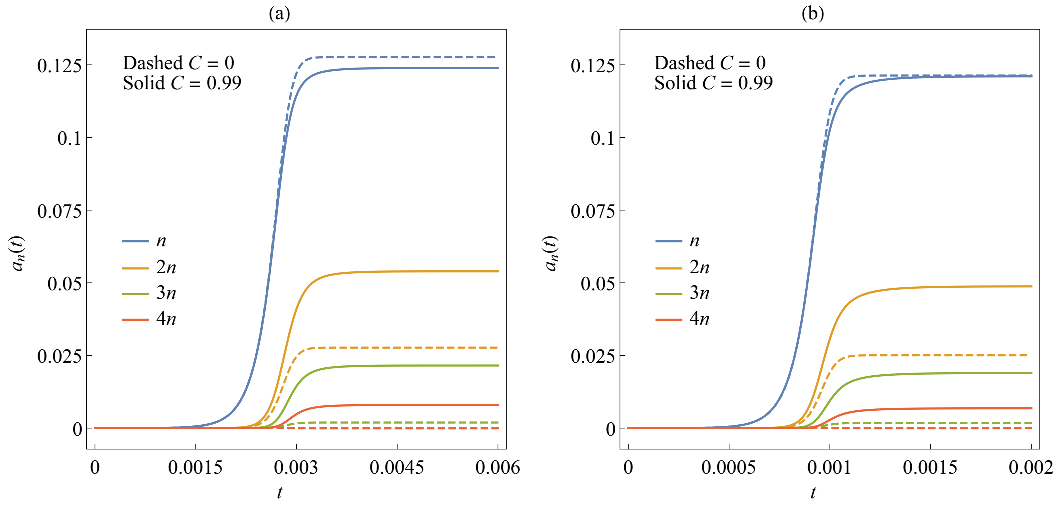

FIG. 7. Time evolution of the perturbation amplitudes $a_n(t)$, $a_{2n}(t)$, $a_{3n}(t)$, and $a_{4n}(t)$ for the patterns depicted in (a) Figs. 6(a)–6(c) for $n = 4$ and (b) Figs. 6(d)–6(f) for $n = 5$. The dashed (solid) curves take the value $C = 0$ ($C = 0.99$). As in the case of elastic interface ferrofluids, here it is also evident that for both values of C the mode amplitudes tend to stationary values.

and due to the stabilizing role of S_0, the resulting fingers will just be a little shorter than the ones obtained when $S_0 = 0$. Therefore, the morphologies revealed in Fig. 6 are quite representative of the general behavior presented by elastic interface MR fluid patterns in the weakly nonlinear stage.

For the sake of completeness and clearness in Fig. 7 we present the time evolution of the cosine perturbation amplitudes $a_n(t)$ for modes n, $2n$, $3n$, and $4n$ for the MR fluid patterns shown in Fig. 6. Figure 7(a) depicts the situations shown in Figs. 6(a) and 6(b), while Fig. 7(b) presents data related to Figs. 6(d) and 6(e). It is reassuring to verify that all mode amplitudes eventually reach stationary values also in the situations involving elastic interface MR fluids. This substantiates the practical relevance of our second-order solutions for the elastic interface MR pattern-forming process, in the sense that the behaviors observed in Fig. 6 are not related to spurious transient effects.

Figure 8 explores some additional information about the elastic interface MR fluid finger shape behavior by analyzing the variation of the curvature of a fingertip κ for a large range of values of the bending rigidity fraction C ($0 \leqslant C \leqslant 0.99$). Similar to what we have done in Fig. 4, here we also examine how the magnetoelastic number N_B impacts the fingertip curvature, and Fig. 8 is plotted for three values of N_B: 58, 64, and 70. The data illustrated in Fig. 8 utilize the physical parameters associated with the fourfold MR fluid structures portrayed in Figs. 6(a)–6(c). As in the case of Fig. 4, one promptly notices that although large values of C and N_B favor the rising of sharper fingers, if the magnitude of C is high enough, the role of the bending rigidity fraction is prevalent and determines the behavior of the fingertip. Many of the same conclusions are reached if Fig. 8 is plotted for the fivefold patterns illustrated in Figs. 6(d)–6(f).

As we did in Sec. III A, now we study the morphological differences between a typical elastic interface MR fluid pattern and the corresponding and more commonly examined situation in which the MR fluid fingering structures are formed under the absence of elastic effects so that at the interface there is a surface tension [18,19]. We do this with the help of Fig. 9, where we also examine the impact of the number of participating Fourier modes N on the shape of second-order stationary state patterns.

Figures 9(a) and 9(b) reproduce typical fivefold elastic interface MR fluid, stationary patterns for $C = 0$, $\chi = 0.45$, $N_B = 15000$, $S_0 = 0$, and $S = 5500$. Additionally, Figs. 9(c) and 9(d) illustrate the characteristic fivefold stationary patterns for the situation with no bending rigidity but with

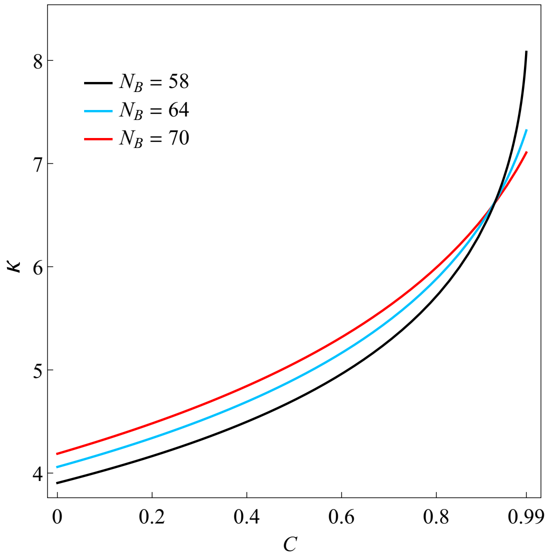

FIG. 8. Variation of the fingertip curvature κ in terms of C, for three values of the magnetoelastic number N_B: 58, 64, and 70. The remaining physical parameters are identical to the ones used in the fourfold MR fluid patterns shown in Figs. 6(a)–6(c).

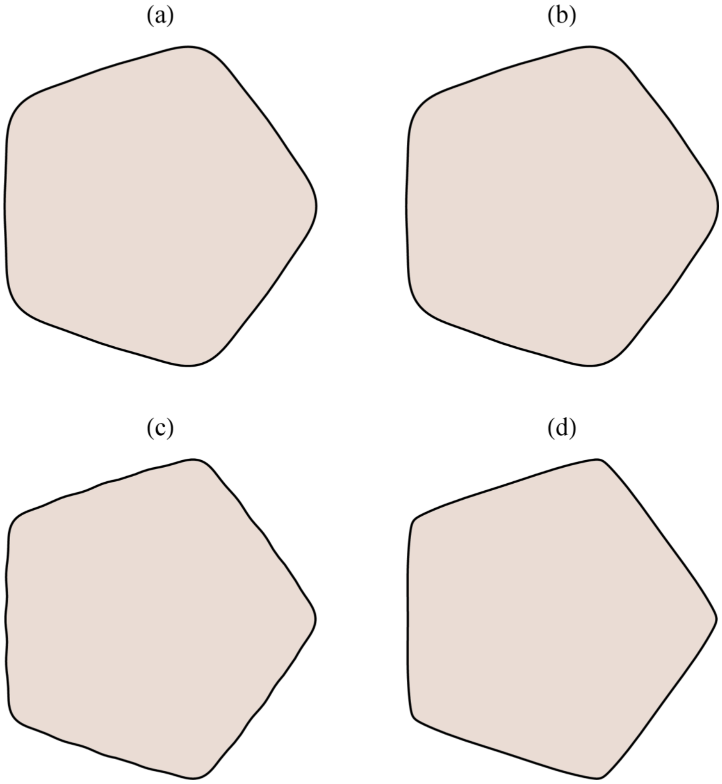

FIG. 9. Comparison of the typical MR fluid, stationary patterned shapes when at the boundary separating the fluids there is (a) and (b) an elastic bending rigidity or (c) and (d) an interfacial surface tension. These patterns are produced by using (a) and (c) four ($N = 4$) and (b) and (d) 40 ($N = 40$) participating modes.

surface tension, for which $\chi = 0.45$, $N_B^{\sigma} = 195$, $S_0 = 0$, and $S = 60$. The shapes reproduced in Figs. 9(a) and 9(c) are obtained by considering the coupling of four participating Fourier modes (n, $2n$, $3n$, and $4n$), while for the interfaces shown in Figs. 9(b) and 9(d) 40 participating modes are utilized ($n, 2n, 3n, \dots, 40n$). First, one rapidly realizes that the elastic interface MR fluid patterns represented in Figs. 9(a) and 9(b) are virtually identical, irrespective of the fact that the number of participating modes N is very different. Similar to the case of elastic interface ferrofluids discussed in Figs. 5(a) and 5(b), this indicates that the use of only four modes is already sufficient to accurately reproduce the shape of such an elastic interface MR fluid pattern. Nevertheless, the surface tension patterns appearing in Figs. 9(c) and 9(d) are not exactly the same. On one hand, the surface tension pattern generated for $N = 4$ [Fig. 9(c)] presents rounded fingertips at the vertices and small undulations along the edges of the polygonal structure. On the other hand, the surface tension pattern obtained when $N = 40$ [Fig. 9(d)] has more pointy fingertips and fairly straight edges. Thus, despite the general similarity in the shape of the surface tension patterns for $N = 4$ and $N = 40$, it is clear that the morphologies of the patterns are modified if more participating modes are considered. Finally, by comparing the elastic interface MR fluid pattern [Fig. 5(b)] with its related surface tension pattern [Fig. 5(d)], both considering the interplay of 40 participating Fourier modes, the morphological distinction between them is apparent: The elastic interface MR fluid pattern [Fig. 5(b)] has a more inflated body containing rounded fingers and the surface tension MR fluid pattern [Fig. 5(d)] presents an even more characteristic polygonal shape having straighter edges and acute fingers at their vertices. The results discussed in Fig. 9 as well as in Fig. 5 highlight the effects of substituting surface by bending rigidity, reinforcing the significance of studying the confined magnetoelastic structures presented in this work.

IV. CONCLUSION

This work has presented a theoretical study of instabilities of an elastic interface separating a magnetic-field-responsive fluid (ferrofluid, or MR fluid) and a nonmagnetic fluid. These fluids are confined in an effectively two-dimensional Hele-Shaw cell and subjected to an applied radial magnetic field. As it occurs in the case of nonmagnetic reactive fluids [24,35,37], our magnetoelastic setup considers that the elastic interface is the result of a chemical reaction that takes place when magnetic and nonmagnetic fluids are put into contact. Additionally, the elastic interface is modeled as having a curvature-dependent bending rigidity.

By employing a second-order mode-coupling approach, we derived a nonlinear differential equation that describes the time evolution of the interfacial perturbation amplitudes. A key feature of our second-order perturbative scheme is the fact that through the coupling of the appropriate Fourier modes, one is able to extract relevant information about the morphology of the interface. In this framework, and by using just a few participating Fourier modes (the fundamental n and its harmonics $2n$, $3n$, and $4n$), we have been able to study how the interplay of magnetic, elastic, and yield stress effects impacts the shape of the emerging elastic interface magnetic fluid patterns at the early nonlinear regime.

We have found that starlike patterns are produced in the elastic interface ferrofluid case, while polygonal-like structures are generated in the elastic MR fluid situation. We have shown that the shapes and lengths of the fingering structures are determined by the combined action of the bending rigidity fraction parameter C and the magnetoelastic number N_B. However, the longest and sharpest fingers tend to arise for larger values of C. Moreover, we have checked that the resulting weakly nonlinear magnetoelastic patterns assume stationary configurations already at the lowest nonlinear (second-order) level. Finally, we also have verified that the magnetoelastic pattern-forming structures obtained in this work are indeed different from their usual nonelastic counterparts in which elastic effects are not present, but are replaced by interfacial surface tension.

We hope that our current weakly nonlinear, theoretical investigation will stimulate interest in the further study of this class of still poorly exploited magnetoelastic problems in Hele-Shaw cells. A possible extension of this work could try to tackle the fully nonlinear aspects of the problem through numerical simulations in the same spirit of Ref. [37]. In addition to possibly checking our weakly nonlinear predictions, such advanced time stage simulations could reveal even more interesting and complex pattern-forming phenomena. Of course, the development of laboratory experiments involving reactive magnetic and nonmagnetic confined fluids subjected to a radial magnetic field could also explore more thoroughly how the resulting elastic magnetic fluid patterns behave in linear, weakly nonlinear, and fully nonlinear time regimes.

ACKNOWLEDGMENTS

J.A.M. thanks CNPq (Brazilian Research Council) for financial support under Grant No. 304821/2015-2. Useful discussions with Sérgio Lira and Roberto Dias are gratefully acknowledged.

APPENDIX: FUNCTIONS APPEARING IN THE MODE-COUPLING TERM $F(n, m)$

This Appendix presents the expressions for the functions $B_1(n, m)$, $B_2(n, m)$, $B_3(n, m)$, and $B_4(n, m)$ which appear in Eq. (19),

$$B_1(n,m) = -3 + \tfrac{15}{4}m(n-m) + 10(n-m)^2 - \tfrac{9}{2}m^2(n-m)^2 - 6m(n-m)^3 - 4(n-m)^4, \tag{A1}$$

$$\begin{aligned} B_2(n,m) = {} & \tfrac{39}{2} - 30m(n-m) - 71(n-m)^2 + \tfrac{81}{2}m^2(n-m)^2 + 54m(n-m)^3 \\ & + 32(n-m)^4 - 12m^2(n-m)^4 - 12m^3(n-m)^3, \end{aligned} \tag{A2}$$

$$\begin{aligned} B_3(n,m) = {} & -14 + 25m(n-m) + 54(n-m)^2 - 36m^2(n-m)^2 - 48m(n-m)^3 \\ & - 26(n-m)^4 + 18m^2(n-m)^4 + 18m^3(n-m)^3, \end{aligned} \tag{A3}$$

and

$$\begin{aligned} B_4(n,m) = {} & 1 - 2m(n-m) - 4(n-m)^2 + 3m^2(n-m)^2 + 4m(n-m)^3 \\ & + 2(n-m)^4 - 2m^2(n-m)^4 - 2m^3(n-m)^3. \end{aligned} \tag{A4}$$

[1] R. E. Rosensweig, *Ferrohydrodynamics* (Cambridge University Press, Cambridge, 1985).

[2] E. Blums, A. Cebers, and M. M. Maiorov, *Magnetic Fluids* (de Gruyter, New York, 1997).

[3] J. M. Ginder, Behavior of magnetorheological fluids, MRS Bull. **23**, 26 (1998).

[4] G. Bossis, S. Lacis, A. Meunier, and O. Volkova, Magnetorheological fluids, J. Magn. Magn. Mater. **252**, 224 (2002).

[5] S. Genç and P. P. Phulé, Rheological properties of magnetorheological fluids, Smart Mater. Struct. **11**, 140 (2002).

[6] P. Coussot, Yield stress fluid flows: A review of experimental data, J. Non-Newtonian Fluid Mech. **211**, 31 (2014).

[7] S. A. Lira and J. A. Miranda, Field-controlled adhesion in confined magnetorheological fluids, Phys. Rev. E **80**, 046313 (2009).

[8] R. H. Ewoldt, P. Tourkine, G. H. McKinley, and A. E. Hosoi, Controllable adhesion using field-activated fluids, Phys. Fluids **23**, 073104 (2011).

[9] See, for instance, D. Andelman and R. E. Rosensweig, Modulated phases: Review and recent results, J. Phys. Chem. B **113**, 3785 (2009); J.-C. Bacri and F. Elias, in *Morphogenesis-Origins of Patterns and Shapes*, edited by P. Bourgine and A. Lesne (Springer, New York, 2011); I. Torres-Díaz and C. Rinaldi, Recent progress in ferrofluids research: Novel applications of magnetically controllable and tunable fluids, Soft Matter **10**, 8584 (2014).

[10] J. White, J. Oakley, M. Anderson, and R. Bonazza, Experimental measurements of the nonlinear Rayleigh-Taylor instability using a magnetorheological fluid, Phys. Rev. E **81**, 026303 (2010).

[11] P. G. Saffman and G. I. Taylor, The penetration of a fluid into a porous medium or Hele-Shaw cell containing a more viscous liquid, Proc. R. Soc. London Ser. A **245**, 312 (1958).

[12] For review articles on Hele-Shaw flows see D. Bensimon, L. P. Kadanoff, S. Liang, B. I. Shraiman, and C. Tang, Viscous flows in two dimensions, Rev. Mod. Phys. **58**, 977 (1986); G. M. Homsy, Viscous fingering in porous media, Annu. Rev. Fluid Mech. **19**, 271 (1987); K. V. McCloud and J. V. Maher, Experimental perturbations to Saffman-Taylor flow, Phys. Rep. **260**, 139 (1995); J. Casademunt, Viscous fingering as a paradigm of interfacial pattern formation: Recent results and new challenges, Chaos **14**, 809 (2004).

[13] A. O. Tsebers and M. M. Maiorov, Magnetostatic instabilities in plane layers of magnetizable liquids, Magnetohydrodynamics **16**, 21 (1980).

[14] A. O. Tsebers, Dynamics of magnetostatic instabilities, Magnetohydrodynamics **17**, 113 (1981).

[15] D. P. Jackson, R. E. Goldstein, and A. O. Cebers, Hydrodynamics of fingering instabilities in dipolar fluids, Phys. Rev. E **50**, 298 (1994).

[16] J. Kent-Dobias and A. J. Bernoff, Energy-driven pattern formation in planar dipole-dipole systems in the presence of weak noise, Phys. Rev. E **91**, 032919 (2015).

[17] R. M. Oliveira, J. A. Miranda, and E. S. G. Leandro, Ferrofluid patterns in a radial magnetic field: Linear stability, nonlinear dynamics, and exact solutions, Phys. Rev. E **77**, 016304 (2008).

[18] S. A. Lira, J. A. Miranda, and R. M. Oliveira, Field-induced patterns in confined magnetorheological fluids, Phys. Rev. E **81**, 046303 (2010).

[19] P. H. A. Anjos, S. A. Lira, and J. A. Miranda, Fingering patterns in magnetic fluids: Perturbative solutions and the stability of exact stationary shapes, Phys. Rev. Fluids **3**, 044002 (2018).

[20] S. Elborai, D.-K. Kim, X. He, S.-H. Lee, S. Rhodes, and M. Zahn, Self-forming, quasi-two-dimensional, magnetic-fluid patterns with applied in-plane-rotating and dc-axial magnetic fields, J. Appl. Phys. **97**, 10Q303 (2005).

[21] E. O. Dias and J. A. Miranda, Azimuthal field instability in a confined ferrofluid, Phys. Rev. E **91**, 023020 (2015).

[22] E. O. Dias, S. A. Lira, and J. A. Miranda, Interfacial patterns in magnetorheological fluids: Azimuthal field-induced structures, Phys. Rev. E **92**, 023003 (2015).

[23] C.-Y. Chen and T.-S. Lin, in *Advances in Computational Fluid-Structure Interaction and Flow Simulation*, edited by Y. Bazilevs and K. Takizawa (Springer Nature, Basel, 2016).

[24] T. Podgorski, M. C. Sostarecz, S. Zorman, and A. Belmonte, Fingering instabilities of a reactive micellar interface, Phys. Rev. E **76**, 016202 (2007).

[25] J. Fernandez and G. M. Homsy, Viscous fingering with chemical reaction: Effect of *in-situ* production of surfactants, J. Fluid Mech. **480**, 267 (2003).

[26] Y. Nagatsu, K. Matsuda, Y. Kato, and Y. Tada, Experimental study on miscible viscous fingering involving viscosity changes induced by variations in chemical species concentrations due to chemical reactions, J. Fluid Mech. **571**, 475 (2007).

[27] Y. Nagatsu, C. Iguchi, K. Matsuda, Y. Kato, and Y. Tada, Miscible viscous fingering involving viscosity changes of the displacing fluid by chemical reactions, Phys. Fluids **22**, 024101 (2010).

[28] Z. Niroobakhsh, M. Litman, and A. Belmonte, Flow instabilities due to the interfacial formation of surfactant–fatty acid material in a Hele-Shaw cell, Phys. Rev. E **96**, 053102 (2017).

[29] F. Haudin, J. H. E. Cartwright, F. Brau, and A. De Wit, Spiral precipitation patterns in confined chemical gardens, Proc. Natl. Acad. Sci. USA **111**, 17363 (2014).

[30] Y. Nagatsu, Y. Ishii, Y. Tada, and A. De Wit, Hydrodynamic Fingering Instability Induced by a Precipitation Reaction, Phys. Rev. Lett. **113**, 024502 (2014).

[31] F. Haudin and A. De Wit, Patterns due to an interplay between viscous and precipitation-driven fingering, Phys. Fluids **27**, 113101 (2015).

[32] F. Haudin, V. Brasiliense, J. H. Cartwright, F. Brau, and A. De Wit, Genericity of confined chemical garden patterns with regard to changes in the reactants, Phys. Chem. Chem. Phys. **17**, 12804 (2015).

[33] Y. Nagatsu, A. Hayashi, M. Ban, Y. Kato, and Y. Tada, Spiral pattern in a radial displacement involving a reaction-producing gel, Phys. Rev. E **78**, 026307 (2008).

[34] Y. Sumino, H. Kitahata, Y. Shinohara, N. L. Yamada, and H. Seto, Formation of a multiscale aggregate structure through spontaneous blebbing of an interface, Langmuir **28**, 3378 (2012).

[35] A. He, J. S. Lowengrub, and A. Belmonte, Modeling an elastic fingering instability in a reactive Hele-Shaw flow, SIAM J. Appl. Math. **72**, 842 (2012).

[36] G. D. Carvalho, J. A. Miranda, and H. Gadêlha, Interfacial elastic fingering in Hele-Shaw cells: A weakly nonlinear study, Phys. Rev. E **88**, 053006 (2013).

[37] M. Zhao, A. Belmonte, S. Li, X. Li, and J. S. Lowengrub, Nonlinear simulations of elastic fingering in a Hele-Shaw cell, J. Comput. Appl. Math. **307**, 394 (2016).

[38] P. H. A. Anjos, G. D. Carvalho, S. A. Lira, and J. A. Miranda, Wrinkling and folding patterns in a confined ferrofluid droplet with an elastic interface, Phys. Rev. E **99**, 022608 (2019).

[39] J. A. Miranda and M. Widom, Radial fingering in a Hele-Shaw cell: A weakly nonlinear analysis, Physica D **120**, 315 (1998).

[40] L. Gordillo and E. Knobloch, Fluid-supported elastic sheet under compression: Multifold solutions, Phys. Rev. E **99**, 043001 (2019).

[41] T. P. Meyrath, Experiments with Bose-Einstein condensation in an optical box, Ph.D. thesis, The University of Texas at Austin, 2005.

[42] T. H. Bergeman, G. Erez, and H. J. Metcalf, Magnetostatic trapping field for neutral atoms, Phys. Rev. A **35**, 1535 (1987).

[43] J. G. E. Harris, R. A. Michniak, S. V. Nguyen, W. C. Campbell, D. Egorov, S. E. Maxwell, L. D. van Buuren, and J. M. Doyle, Deep superconducting magnetic traps for neutral atoms and molecules, Rev. Sci. Instrum. **75**, 17 (2004).

[44] C.-Y. Chen, Y.-S. Yang, and J. A. Miranda, Miscible ferrofluid patterns in a radial magnetic field, Phys. Rev. E **80**, 016314 (2009).

[45] C.-Y. Chen, W.-L. Wu, and J. A. Miranda, Magnetically induced spreading and pattern selection in thin ferrofluid drops, Phys. Rev. E **82**, 056321 (2010).

[46] R. Aslam and W. Gonzáles-Viñas, Pattern formation in spin-coating of hybrid colloids in different magnetic field configurations, J. Phys. D **52**, 344001 (2019).

[47] G. H. Covey and B. R. Stanmore, Use of the parallel-plate plastometer for the characterisation of viscous fluids with a yield stress, J. Non-Newtonian Fluid Mech. **8**, 249 (1981).

[48] G. K. Batchelor, *An Introduction to Fluid Dynamics* (Cambridge University Press, Cambridge, 2000).

[49] *Fluid-Structure Interactions in Low-Reynolds-Number Flows*, edited by C. Duprat and H. Stone (RSC, Cambridge, 2016).

[50] E. Alvarez-Lacalle, E. Pauné, J. Casademunt, and J. Ortín, Systematic weakly nonlinear analysis of radial viscous fingering, Phys. Rev. E **68**, 026308 (2003).